ROYAL SOCIETY OF CHEMISTRY

EDGE ARTICLE

Check for updates

Facile fabrication of Ni, Fe-doped δ-MnO₂ derived from Prussian blue analogues as an efficient catalyst for stable Li–CO₂ batteries†

Xiaoyang Chen,‡[a] Jian Chen, [ID] ‡[a] Yun Qiao, [ID] *[a] Yun Gao,[b] Siwei Fan,[a] Yijie Liu,[a] Li Li,[a] Yang Liu*[a] and Shulei Chou [ID] *[b]

Rechargeable Li–CO₂ batteries are regarded as an ideal new-generation energy storage system, owing to their high energy density and extraordinary CO₂ capture capability. Developing a suitable cathode to improve the electrochemical performance of Li–CO₂ batteries has always been a research hotspot. Herein, Ni–Fe-δ-MnO₂ nano-flower composites are designed and synthesized by *in situ* etching a Ni–Fe PBA precursor as the cathode for Li–CO₂ batteries. Ni–Fe-δ-MnO₂ nanoflowers composed of ultra-thin nanosheets possess considerable surface spaces, which can not only provide abundant catalytic active sites, but also facilitate the nucleation of discharge products and promote the CO₂ reduction reaction. On the one hand, the introduction of Ni and Fe elements can improve the electrical conductivity of δ-MnO₂. On the other hand, the synergistic catalytic effect between Ni, Fe elements and δ-MnO₂ will greatly enhance the cycling performance and reduce the overpotential of Li–CO₂ batteries. Consequently, the Li–CO₂ battery based on the Ni–Fe-δ-MnO₂ cathode shows a high discharge capacity of 8287 mA h g⁻¹ and can stabilize over 100 cycles at a current density of 100 mA g⁻¹. The work offers a promising guideline to design efficient manganese-based catalysts for Li–CO₂ batteries.

Introduction

Nowadays, the over-dependence on traditional fossil fuels and the continuous release of greenhouse gases (CO₂) have led to serious environmental problems and hindered the sustainable development of the world.[1,2] To reduce carbon emissions or repurpose CO₂, various chemical processes have been adopted to convert CO₂ into value-added carbon compounds, such as methanol, organic materials and plastics.[3–7] However, the conventional CO₂ reduction system usually shows less energy conversion efficiency than the ideal value, due to the complex multi-electron reaction on the surface of the electrode.[8–10] Therefore, direct electrochemical reduction of CO₂ through a new energy storage device is an ideal strategy. Currently, metal–CO₂ batteries, especially Li–CO₂ batteries, show great potential in novel electrochemical CO₂ reduction energy storage systems, due to their high energy density and reversible CO₂ drive.[11,12] Unfortunately, the development and exploration of Li–CO₂ batteries are still in the early stage, and their practical

application is restricted by large polarization, poor cycle stability and low coulombic efficiency.[13–15]

Typically, the widely recognized electrochemical reaction of Li–CO₂ batteries is confirmed to be $4Li + 3CO_2 = 2Li_2CO_3 + C$ ($E = 2.80$ V *vs.* Li/Li⁺).[16,17] However, it is found that Li_2CO_3, the discharge product of Li–CO₂ batteries, is a kind of insulator with a wide band gap, and its decomposition kinetics is slow. As a result, Li_2CO_3, which is difficult to decompose, gradually accumulates on the surface of the cathode during cycling, inducing the coverage on the active sites of the catalyst and thus causing the cell deactivation.[18,19] Therefore, the study of cathodes with high catalytic activity to achieve reversible decomposition of Li_2CO_3 is a key strategy to improve the performance of Li–CO₂ batteries. Noble metal catalysts have been shown to promote the reversible formation and decomposition of Li_2CO_3 at lower potentials, greatly improving the electrochemical performance of Li–CO₂ batteries.[20–24] Nevertheless, their large-scale application is limited due to the high price and scarce reserves of noble metal catalysts.

Transition metal catalysts are considered as good substitutes for noble metal catalysts because of their excellent catalytic activity and relatively low cost.[25–27] Numerous studies have proved that MnO₂ catalyst can effectively promote the CO₂ reduction reaction (CO₂RR) and CO₂ evolution reaction (CO₂ER) processes.[28] In previous studies, Lei *et al.* reported that the α-MnO₂/CNT electrode could provide sufficient active sites for Li_2CO_3 nucleation and CO₂ capture, and the cathode structure

ªSchool of Environmental and Chemical Engineering, Shanghai University, Shanghai 200444, China. E-mail: yunqiao@shu.edu.cn; liuy986@163.com

ᵇInstitute for Carbon Neutralization, College of Chemistry and Materials, Engineering, Wenzhou University, Zhejiang 325035, China. E-mail: chou@wzu.edu.cn

‡ X.-Y. C and J. C. contributed equally to this work.

could be tuned.[29] Similarly, Wang *et al.* successfully synthesized the CNT@MnO$_2$ (Birnessite δ-MnO$_2$) cathode; the as-assembled Li–CO$_2$ batteries exhibited low overpotential and excellent cycle stability with the synergistic effect of δ-MnO$_2$ and CNTs.[30] However, further improvement of MnO$_2$ catalytic activity is restricted by its poor conductivity and limited active sites. Previous results have shown that the electrical conductivity of MnO$_2$ can be improved by modifying its band level and electronic structure through the introduction of atomic doping. Based on these inspirations, Peng *et al.* first applied Co-doped α-MnO$_2$ nanowires for Li–CO$_2$ batteries, achieving a low overpotential of 0.73 V and long cycle performance (500 cycles at 100 mA g^{-1}). They attributed the excellent electrochemical performance to the high conductivity of Co-α-MnO$_2$ nanowires, enhanced specific surface area, and synergistic catalysis of doped Co atoms.[31] However, its irregular pore size and low active specific surface area lead to non-uniform deposition of Li$_2$CO$_3$ and low discharge capacity, which will limit its practical application.

Herein, Ni, Fe co-doped δ-MnO$_2$ (Ni–Fe-δ-MnO$_2$) nanoflowers as a cathode for Li–CO$_2$ batteries were synthesized by *in situ* etching the Ni–Fe PBA precursors *via* a sacrificing-template strategy. Ni–Fe-δ-MnO$_2$ nanoflowers can significantly promote the CO$_2$RR and CO$_2$ER processes and improve the cycle stability of Li–CO$_2$ batteries. These excellent electrochemical properties are attributed to the unique nanoflower structure, abundant exposed surfaces, and a large number of oxygen vacancy defects of Ni–Fe-δ-MnO$_2$. Furthermore, the introduction of Ni and Fe elements can not only improve the conductivity of δ-MnO$_2$, but also significantly promote the reversible formation and decomposition of Li$_2$CO$_3$. Therefore, this work will provide an ideal guidance for the design of efficient Li–CO$_2$ battery cathodes in the future.

Results and discussion

Highly crystalline three-dimensional nanocubes with a uniform diameter of 50 nm were synthesized by the co-precipitation method, and are denoted as Ni–Fe-PBA (Fig. S1a and b†). As shown in Fig. 1, nanoflowers with a diameter of 170 nm are grown vertically and uniformly on the Ni–Fe-PBA template after the hydrothermal process, denoted as the Ni–Fe-δ-MnO$_2$ precursor (Fig. S1c and d†). Subsequently, Ni–Fe-δ-MnO$_2$ was obtained by calcining the Ni–Fe-δ-MnO$_2$ precursor in an Ar atmosphere at 300 °C for 2 h. The X-ray diffraction (XRD) characteristic peaks of Ni–Fe-δ-MnO$_2$ at 12.5°, 25.2°, 37.3°, and 65.6° can be well attributed to the (001), (002), (1ī1), and (020) crystal faces of δ-MnO$_2$ (JCPDS no. 80-1098), as shown in Fig. 2a. Scanning electron microscopy (Fig. 2b and c) revealed that the morphology of Ni–Fe-δ-MnO$_2$ is well maintained compared with that of the Fe-δ-MnO$_2$ precursor, which means that these nanoflowers possess superior stability. Interestingly, the nanoflower structure exposes a large surface, which can provide a large space and rich active sites for the deposition and decomposition of discharge products. Meanwhile, no residues of other PBA-derived precursors are observed in the SEM images, which further indicates that Ni–Fe PBA has been completely etched during the hydrothermal process. Transmission electron microscopy (TEM) was performed to further demonstrate the cubic nanoflower morphology of Ni–Fe-δ-MnO$_2$ (Fig. 2d). It is worth noting that the ultra-thin nanosheets tend to bend and fold, and their thickness can be determined by measuring the folded area. The high-resolution transmission electron microscopy (HRTEM) image displays a lattice spacing of 0.67 nm, corresponding to the (001) plane of Ni–Fe-δ-MnO$_2$ (Fig. 2e). Furthermore, the thickness of the nanosheet is about 2.7 nm, corresponding to Ni–Fe-δ-MnO$_2$ (001) crystal surfaces.[32] Additionally, considerable micropores can be seen in Fig. 2f, which can provide more nucleation regions and oxygen vacancies, conducive to electron transport and nucleation of Li$_2$CO$_3$. The high-angle annular dark field-scanning transmission microscope (HAADF-STEM) image of Ni–Fe-δ-MnO$_2$ in Fig. 2g and the corresponding energy dispersive spectrometer (EDS) elemental mapping in Fig. 2h–l clearly prove the presence of Ni, Fe, Mn, and O elements in the catalyst, which are evenly distributed in Ni–Fe-δ-MnO$_2$ nanoflowers. It is worth noting that the presence of K element was also detected in the EDS spectrum, which was also verified by inductively coupled plasma mass spectrometry (ICP-MS) (Table S1†). This indicates that Ni–Fe-δ-MnO$_2$ contains a certain amount of K$^+$. The presence of K$^+$ can not only improve the structural stability and charge balance of MnO$_2$, but also promote the octahedral effect of MnO$_6$ and the diffusion rate of Li$^+$, which will further enhance the catalytic activities of the CO$_2$RR and CO$_2$ER.[33] The contents of Ni and Fe in Ni–Fe-δ-MnO$_2$ are 7.57 and 4.22 wt%, respectively, which means that Ni and Fe with a mass ratio of 2 : 1 occupy the surroundings of the MnO$_6$ octahedron. Thus, more oxygen vacancies are formed and can enhance the CO$_2$RR.

X-Ray photoelectron spectroscopy (XPS) was used to detect the valence state and electronic structure of Ni–Fe-δ-MnO$_2$, Ni–Fe-δ-MnO$_2$ precursor and δ-MnO$_2$. The XPS full spectra show obvious characteristic peaks of Fe, Ni, Mn, O and K elements (Fig. 3a), which are consistent with the EDS analysis results. As shown in Fig. 3b, the high-resolution Mn 2p XPS spectra exhibit three peaks, which can be divided into Mn^{4+} from MnO$_2$ at 642.2 eV, and the Mn^{3+} peaks at 654.0 and 645.4 eV due to the oxygen defects induced by Mn^{4+} transformation. The high-resolution O 1s XPS spectra of Ni–Fe-δ-MnO$_2$ were deconvoluted into three spin-orbital peaks at 529.46, 530.03, and 531.32 eV, corresponding to the lattice oxygen (O$_1$), oxygen vacancy (O$_2$), and hydroxyl or adsorbed water molecules (O$_3$) of Mn–O bonds (Fig. 3c). Ni–Fe-δ-MnO$_2$ has the highest O$_2$ ratio (45.97%), which further proves abundant oxygen vacancy defects in its structure.[34,35] As shown in Fig. 3d, the main peak of Ni 2p$_{3/2}$ and its satellites at 854.9 and 861.4 eV, and the main peak of Ni 2p$_{1/2}$ and its satellites at 872.2 and 879.3 eV are attributed to nickel in its oxides.[36] Similarly, the Fe 2p spectra (Fig. 3e) can be deconvoluted into five peaks at 710.4/723.5 eV (Fe^{3+}), 712.8/725.8 eV (Fe^{2+}) and 769.2 eV (satellite peaks).[37] The result can further confirm the successful synthesis of Ni–Fe-δ-MnO$_2$. As shown in Fig. 3d and e, both Ni 2p and Fe 2p peaks of Ni–Fe-δ-MnO$_2$ move to the lower binding energy in contrast to that of the Ni–Fe-δ-MnO$_2$ precursor, which can increase the density of the surrounding electron cloud. This phenomenon
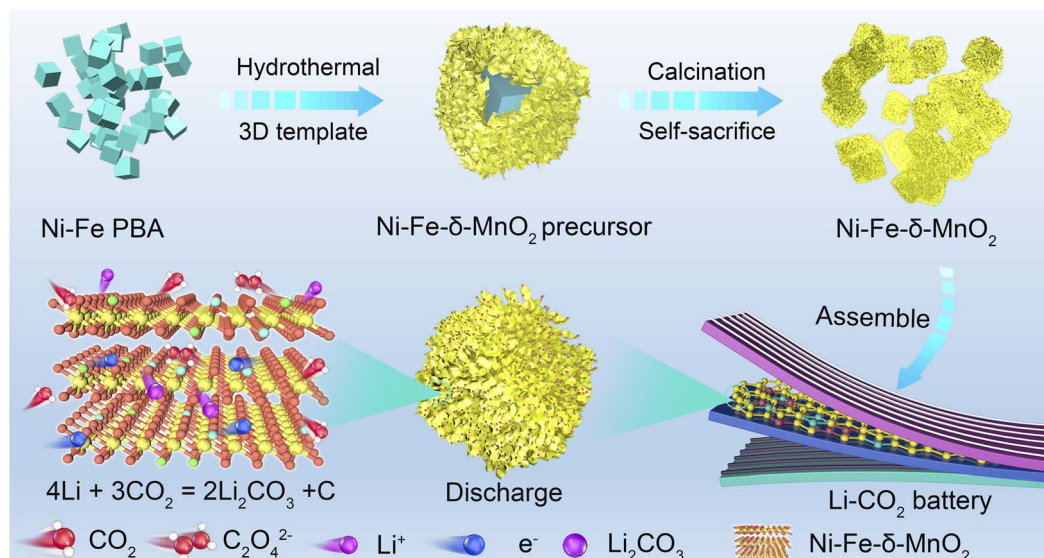
Fig. 1 Schematic illustration for the fabrication of the Ni−Fe-δ-MnO$_2$ cathode.

can be attributed to the co-coordination between Ni/Fe and O atoms in the center of Mn. In this case, this structure can inhibit Jahn–Teller distortion, stabilize the MnO$_2$ structure and expose more active sites. In addition, increasing the electron density of the metal center can enhance the adsorption between the metal center and the intermediate and change the coordination around MnO$_2$ to form more oxygen vacancies. Electron paramagnetic resonance (EPR) spectroscopy was employed to detect the unpaired electrons in Ni–Fe-δ-MnO$_2$. The EPR signal for Ni–Fe-δ-MnO$_2$ is dramatically enhanced in contrast to that of δ-MnO$_2$ and Ni–Fe-δ-MnO$_2$ precursor, which suggests its enhanced oxygen vacancy density (Fig. 3f).[38] Interestingly, the co-doping of Ni and Fe makes Ni–Fe-δ-MnO$_2$ expose more active sites and enhance the oxygen vacancy density through the coordination of adjacent O atoms around Mn, and thus promotes the activities of the CO$_2$RR and CO$_2$ER. Brunauer–
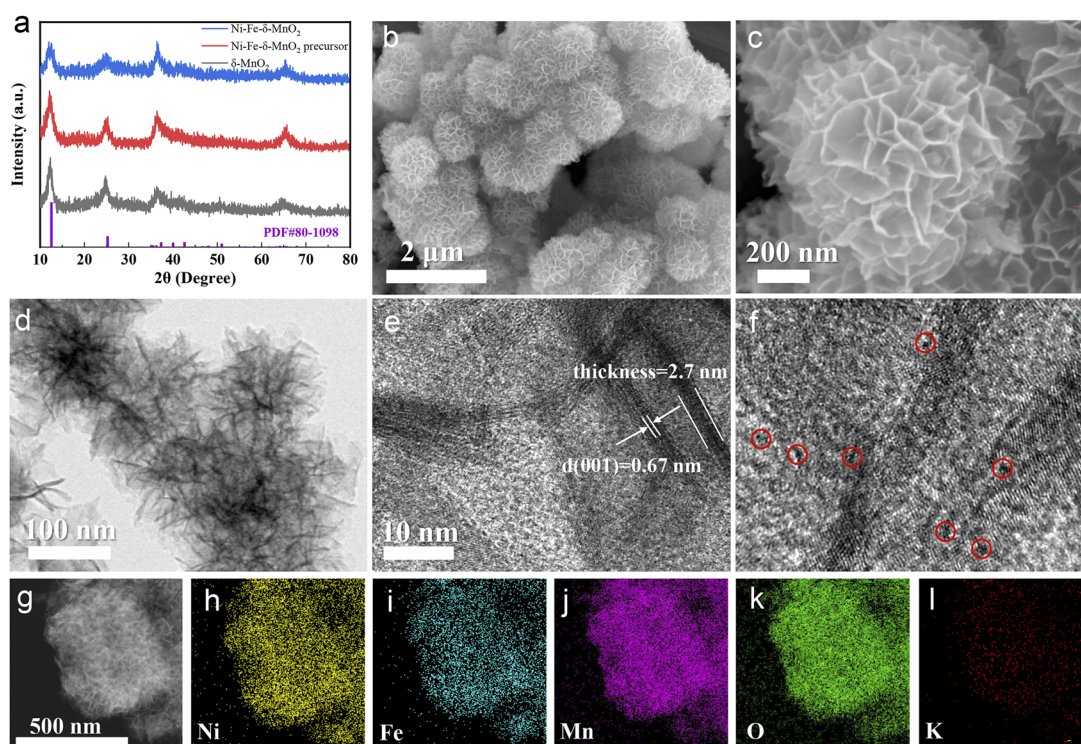

Fig. 2 (a) XRD patterns of δ-MnO$_2$, Ni−Fe-δ-MnO$_2$ precursor and Ni−Fe-δ-MnO$_2$, (b and c) SEM, (d) TEM, (e and f) HRTEM, (g) HAADF–STEM images and corresponding EDS elemental mapping results of (h) Ni, (i) Fe, (j) Mn, (k) O and (l) K elements for Ni−Fe-δ-MnO$_2$.
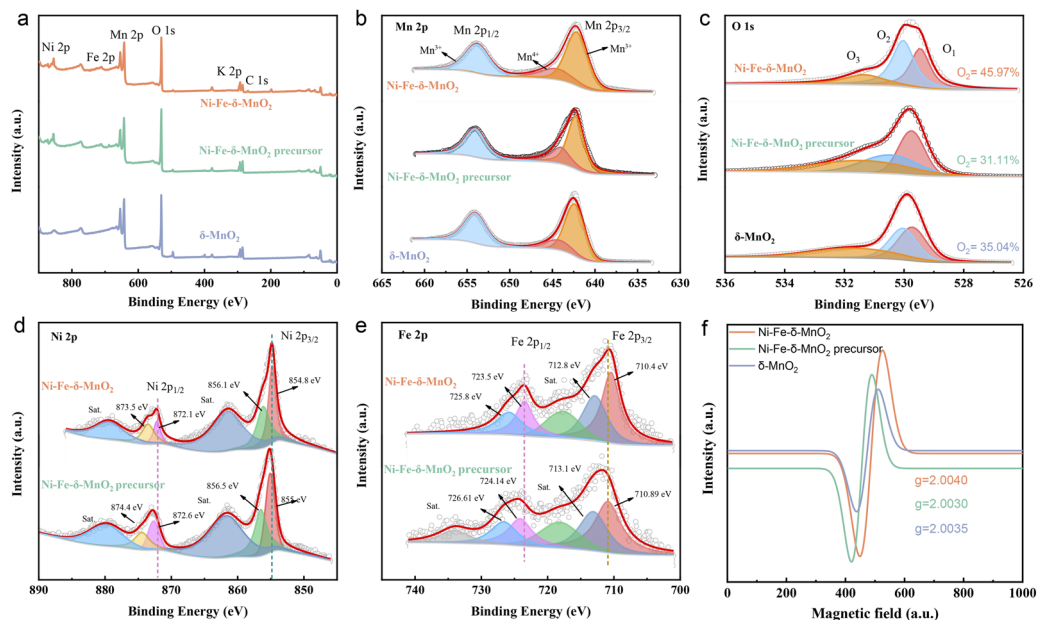
Fig. 3 (a) The survey XPS spectra, high-resolution XPS spectra of (b) Mn 2p, (c) O 1s of Ni–Fe-δ-MnO$_2$, Ni–Fe-δ-MnO$_2$ precursor and δ-MnO$_2$. High-resolution XPS spectra of (d) Ni 2p and (e) Fe 2p of Ni–Fe-δ-MnO$_2$ and Ni–Fe-δ-MnO$_2$ precursor. (f) EPR curves of Ni–Fe-δ-MnO$_2$, Ni–Fe-δ-MnO$_2$ precursor and δ-MnO$_2$.

Emmett–Teller (BET) analysis was applied to investigate the specific surface area of the as-prepared Ni–Fe-δ-MnO$_2$. The nitrogen adsorption and desorption curve (Fig. S2a†) shows that its specific surface area is up to 154.99 m^2 g^{-1} for Ni–Fe-δ-MnO$_2$, meaning that the catalyst can expose considerable active sites and provide sufficient space for the CO$_2$RR process. The pore size distribution results reveal that Ni–Fe-δ-MnO$_2$ possesses a large number of mesoporous structures with pore size in the range of 5.0–33.0 nm (Fig. S2b†). These mesoporous structures can accommodate more deposition of discharge products, enhance the diffusion of CO$_2$ and electrolyte, and expose more active sites. Based on the above analysis, we can conclude that Ni–Fe-δ-MnO$_2$ nanoflowers are successfully prepared. The presence of Ni and Fe elements can improve the electrical conductivity of δ-MnO$_2$. Moreover, their synergistic effect with Mn atoms will further improve the catalytic activity of the cathode. In addition, the large surface area and abundant oxygen vacancy defects for Ni–Fe-δ-MnO$_2$ can greatly enhance the reactivity of the CO$_2$RR and CO$_2$ER. Therefore, Ni–Fe-δ-MnO$_2$ nanoflowers are expected to be an ideal cathode for Li–CO$_2$ batteries.

The electrochemical performance of the Ni–Fe-δ-MnO$_2$ cathode in Li–CO$_2$ batteries was systematically evaluated. As shown in Fig. S3a,† the Ni–Fe-δ-MnO$_2$ cathode shows more obvious reduction and oxidation peaks in a CO$_2$ atmosphere than in an Ar atmosphere. In addition, Fig. S3b† reveals that the discharge capacity of the Ni–Fe-δ-MnO$_2$ cathode is 8287 mA h g^{-1}, which is 2.1 times that of the δ-MnO$_2$ cathode (3923 mA h g^{-1}), suggesting that the Ni–Fe-δ-MnO$_2$ cathode possesses a relatively better catalytic activity for the CO$_2$RR. In order to investigate the stability of the Li–CO$_2$ battery based on the Ni–Fe-δ-MnO$_2$ cathode, charge–discharge tests were

conducted at a current density of 100 mA g^{-1} with a cutoff capacity of 1000 mA h g^{-1}. Fig. 4a and b display the charge and discharge cycles of Ni–Fe-δ-MnO$_2$ and δ-MnO$_2$ cathodes. The Li–CO$_2$ battery with Ni–Fe-δ-MnO$_2$ as the cathode can stabilize for 100 cycles, and its overpotential drops to 1.32 V (Fig. 4a). The charge terminal voltage remains below 4.2 V despite a slight increase after 100 cycles. As a contrast, we also investigated the cycle performance of δ-MnO$_2$ under the same test conditions, as shown in Fig. 4b. It is obvious that δ-MnO$_2$ exhibits extremely poor cycle stability. After 60 cycles, the voltage of its charging platform begins to gradually decrease. Unfortunately, both the terminal charge and discharge voltages reach the cut-off voltage (2.0 and 4.5 V) after 90 cycles. By comparing the discharge and charge terminal voltages of δ-MnO$_2$ and Ni–Fe-δ-MnO$_2$ (Fig. 4c), it can be clearly seen that the Ni–Fe-δ-MnO$_2$ exhibits much better cycle stability than δ-MnO$_2$. In addition, the overpotential of the Ni–Fe-δ-MnO$_2$ cathode is always lower than that of δ-MnO$_2$. Furthermore, we compared the overpotentials of the two cathodes at the 10th cycle (Fig. 4d). Compared with δ-MnO$_2$, the overpotential of the Ni–Fe-δ-MnO$_2$ is decreased by 0.23 V, further indicating that the introduction of Ni and Fe elements can significantly improve the catalytic activity of δ-MnO$_2$.

Fig. 4e exhibits the charge–discharge curves of the Li–CO$_2$ battery with Ni–Fe-δ-MnO$_2$ as the cathode at different current densities. When the current density increases from 400 to 1000 mA g^{-1}, the charge terminal voltage increases by only 0.13 V. The charge terminal voltage of Ni–Fe-δ-MnO$_2$ is only 4.43 V (<4.5 V) even at the current density of 1000 mA g^{-1}, indicating that the Ni–Fe-δ-MnO$_2$ electrode can still maintain excellent CO$_2$ER activity even at a higher current density. Furthermore, the electrochemical performance of the Ni–Fe-δ-MnO$_2$ cathode was compared with that of other Mn-based and related transition
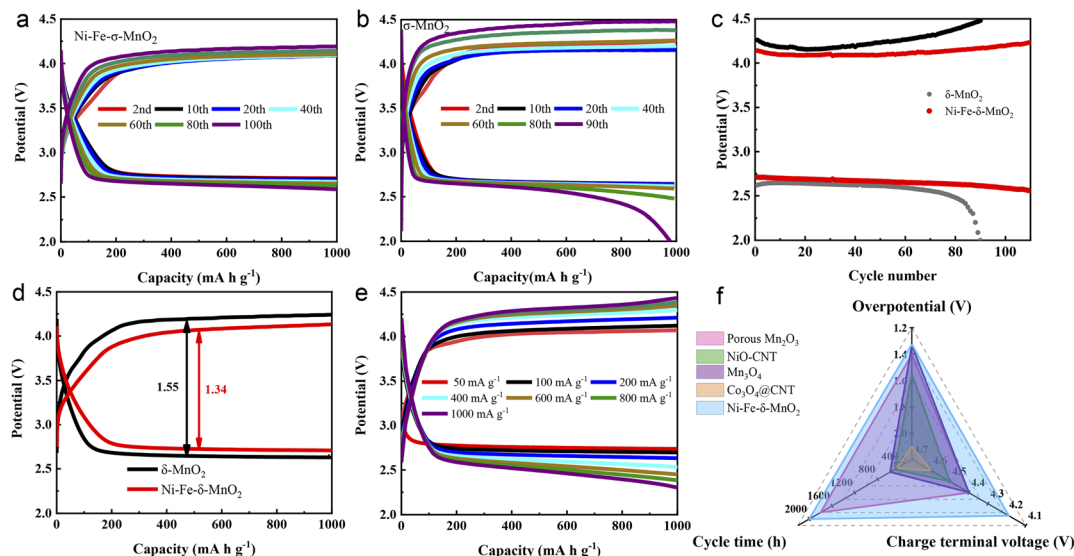
Fig. 4 The discharge and charge curves of (a) Ni–Fe-δ-MnO$_2$ and (b) δ-MnO$_2$ at 100 mA g^{-1} with a limited capacity of 1000 mA g^{-1}. (c) The discharge and charge terminal voltages of Ni–Fe-δ-MnO$_2$ and δ-MnO$_2$ upon cycling, (d) the overpotential comparison for the two cathodes at the 10th cycle. (e) The discharge and charge profiles of the Ni–Fe-δ-MnO$_2$ cathode at different current densities. (f) Comparison of the electrochemical properties of the Ni–Fe-δ-MnO$_2$ cathode and manganese based or other transition metal oxides.

metal catalysts. The radar diagram in Fig. 4f demonstrates that the Ni–Fe-δ-MnO$_2$ cathode endows obvious advantages in terms of cycle time, overpotential and charge terminal voltage.[39–42] These results indicate that Ni–Fe-δ-MnO$_2$ can improve the catalytic activities of the CO$_2$RR and CO$_2$ER, and thus significantly enhance the cycle stability of Li–CO$_2$ batteries.

In order to further explore the mechanism of the excellent electrochemical performance of the Ni–Fe-δ-MnO$_2$ cathode in a Li–CO$_2$ battery, SEM, XPS, *in situ* Raman and Fourier transform infrared (FTIR) spectroscopies were performed to systematically characterize the formation and decomposition of discharge products during the cycling processes. Fig. S6† displays the morphologies and structures of the Ni–Fe-δ-MnO$_2$ cathode at the discharged and recharged states. As shown in Fig. S6a,† discharge products with a flake morphology densely cover on the surface of the entire electrode after the first discharge process. Fortunately, the electrode returns to its pristine morphology, and the carbon nanotubes wrapped around its surface are also exposed after recharging (Fig. S6b†), indicating the reversible formation and decomposition of the discharge products. This result proves that the Ni–Fe-δ-MnO$_2$ electrode possesses excellent reversibility for the formation and decomposition of discharge products. In order to further verify the composition of the discharge products and the reversibility of the Ni–Fe-δ-MnO$_2$ electrode, the XPS spectrum was recorded. As shown in Fig. 5a, the high-resolution C 1s spectra can be deconvoluted into four distinct characteristic peaks at 284.96, 286.78, 290.45 and 293.53 eV after discharge, wherein the characteristic peak at 290.45 eV corresponds to the O–C=O bond of Li$_2$CO$_3$, indicating the existence of Li$_2$CO$_3$ as the discharge product. Importantly, this characteristic peak almost completely disappears after the subsequent recharging

(Fig. 5b), demonstrating the reversibility of the discharge product. Fig. 5c shows the FTIR spectra of the pristine, discharged and recharged Ni–Fe-δ-MnO$_2$ cathodes. The discharged electrode exhibits three new peaks at 865, 1408 and 1476 cm^{-1}, compared with the pristine electrode, which are consistent with the standard spectrum of commercial Li$_2$CO$_3$.[43] Similarly, the characteristic peaks of Li$_2$CO$_3$ almost completely disappear in the subsequent recharging process, which is consistent with the XPS results. Moreover, we further investigated the electrochemical behaviour of the discharge product Li$_2$CO$_3$ in the whole charge and discharge processes by *in situ* Raman spectroscopy. As shown in Fig. 5d, the characteristic peaks of MnO$_2$ (633 cm^{-1}), D band (1343 cm^{-1}) and G band (1574 cm^{-1}) of carbon can be observed in the Raman spectra at the initial discharge stage. As the discharge progresses, the peak intensities of Li$_2$CO$_3$ (1081 cm^{-1}), D and G bands continuously increase, which can be attributed to the formation of discharge products (Li$_2$CO$_3$ and C).[44,45] In addition, the I_D/I_G ratio gradually decreases with the continuous discharge process, indicating that the C product possesses a high degree of graphitization. Noteworthily, higher graphitization is conducive to electron transfer and decomposition of discharge products, as the gradual weakening and eventual disappearance of Li$_2$CO$_3$ and C in the *in situ* Raman spectra during the subsequent charging process proves the complete decomposition of discharge products.[46] The corresponding 2D contour map in Fig. 5e further intuitively reflects this trend of evolution. These results fully demonstrate the reversible formation and decomposition of Li$_2$CO$_3$ during the cycling processes and the excellent catalytic activity of the Ni–Fe-δ-MnO$_2$ electrode for the CO$_2$RR and CO$_2$ER processes.[47] Besides, we can also notice that the characteristic peak of MnO$_2$ gradually disappears during the
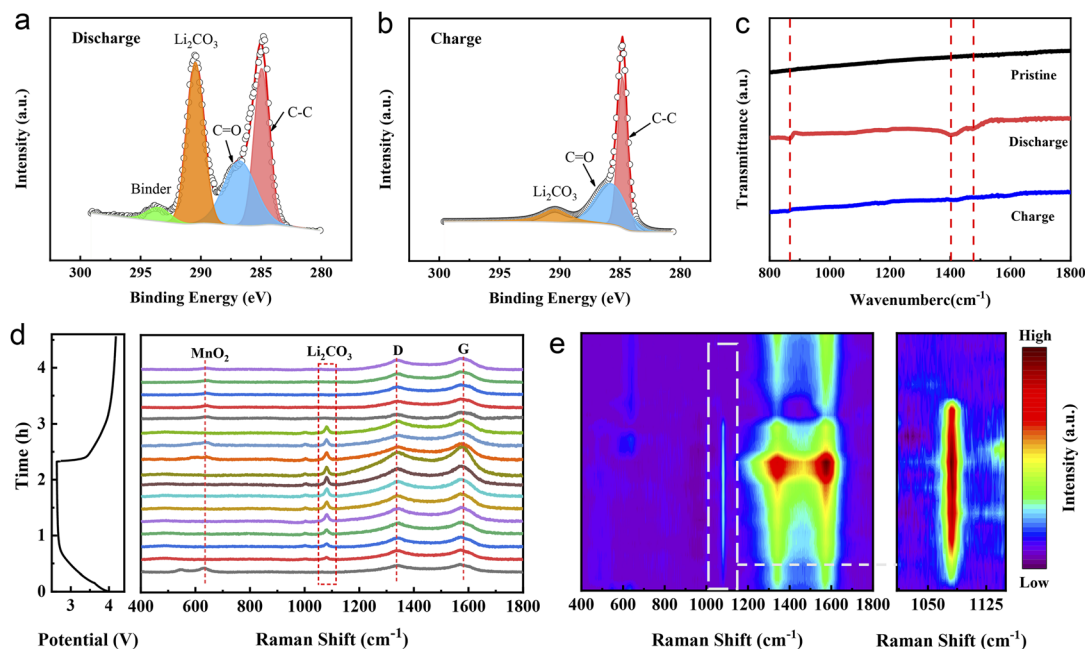
Fig. 5   The *ex situ* and *in situ* characterizations of the Ni–Fe-δ-MnO$_2$ cathode in Li–CO$_2$ batteries. XPS spectra of C 1s after (a) discharge and (b) charge processes. (c) FTIR spectra of the pristine, discharged and charged cathodes. (d) *In situ* Raman spectra and (e) the corresponding 2D contour plots of the Ni–Fe-δ-MnO$_2$ cathode.

discharge stage, which may be due to the coverage of Li$_2$CO$_3$ on the surface of the Ni–Fe-δ-MnO$_2$ electrode, which affects the detected signal of MnO$_2$. It is worth noting that the characteristic peak of MnO$_2$ appears with the gradual disappearance of Li$_2$CO$_3$, which is exactly opposite to the evolution trend of Li$_2$CO$_3$ after recharging. Furthermore, the existence of the MnO$_2$ signal after charging also indicates the stability of the Ni–Fe-δ-MnO$_2$ electrode. Based on the above results, we can conclude that Ni–Fe-δ-MnO$_2$ can promote not only the transport of electrons and Li$^+$ *via* the four-electron interaction but also the nucleation and reversible decomposition of Li$_2$CO$_3$, which could improve its catalytic performance.

Conclusions

In summary, Ni–Fe-doped δ-MnO$_2$ nanoflowers (Ni–Fe-δ-MnO$_2$) are designed and synthesized by etching a Ni–Fe-δ-MnO$_2$ precursor using the sacrificial template method. The Ni–Fe-δ-MnO$_2$ nanoflowers composed of ultra-thin nanosheets possess considerable surface spaces, which can not only provide abundant catalytic active sites, but also facilitate the nucleation of discharge products and promote the CO$_2$ reduction reaction. In addition, the introduction of Ni and Fe elements could improve the electrical conductivity of δ-MnO$_2$. It is worth noting that their synergistic catalytic effect with δ-MnO$_2$ could greatly enhance the cycling performance and reduce the overpotential of the Li–CO$_2$ battery. Due to these advantages, the Li–CO$_2$ battery with the Ni–Fe-δ-MnO$_2$ cathode delivers the highest discharge capacity of 8287 mA h g^{-1} at the current density of 100 mA g^{-1}, which is 2.1 times that of the bare δ-MnO$_2$. Additionally, the Li–CO$_2$ battery based on the Ni–Fe-δ-MnO$_2$ cathode

can achieve a low overpotential of 1.32 V and outstanding cycle performance of 100 cycles. This work provides a reference direction for the design of highly efficient multi-atom co-catalysts in the future.

Data availability

Synthetic procedures, experimental details, and characterization data are available in the ESI.†

Author contributions

Y. Q., Y. L. and S. L. C. proposed the concept and supervised the work; X. Y. C. and J. C. designed the experiments and wrote the paper; S. W. F., Y. G., and Y. J. L. contributed to the discussion and provided suggestions. Y. J. L. helped to analyze the data; L. L. helped to summarize the data. All authors have discussed the results, drafted the manuscript and approved the final version of the manuscript.

Conflicts of interest

There are no conflicts to declare.

Acknowledgements

Notes and references

1 S. Ren, D. Joulié, D. Salvatore, K. Torbensen, M. Wang, M. Robert and C. P. Berlinguette, *Science*, 2019, **365**, 367.

2 Y. Zhou, F. Che, M. Liu, C. Zou, Z. Liang, P. de Luna, H. Yuan, J. Li, Z. Wang, H. Xie, H. Li, P. Chen, E. Bladt, R. Quintero-Bermudez, T.-K. Sham, S. Bals, J. Hofkens, D. Sinton, G. Chen and E. H. Sargent, *Nat. Chem.*, 2019, **11**, 1167.

3 K. S. Lackner, *Science*, 2003, **300**, 1677.

4 S. A. Theofanidis, A. N. Antzaras and A. A. Lemonidou, *Curr. Opin. Chem. Eng.*, 2023, **39**, 100902.

5 J. Zhang, R. Yin, Q. Shao, T. Zhu and X. Huang, *Angew. Chem., Int. Ed.*, 2019, **58**, 5609.

6 U. Ulmer, T. Dingle, P. N. Duchesne, R. H. Morris, A. Tavasoli, T. Wood and G. A. Ozin, *Nat. Commun.*, 2019, **10**, 3169.

7 I. Sullivan, A. Goryachev, I. A. Digdaya, X. Li, H. A. Atwater, D. A. Vermaas and C. Xiang, *Nat. Catal.*, 2021, **4**, 952.

8 R. Zhao, P. Ding, P. Wei, L. Zhang, Q. Liu, Y. Luo, T. Li, S. Lu, X. Shi, S. Gao, A. M. Asiri, Z. Wang and X. Sun, *Adv. Funct. Mater.*, 2021, **31**, 2009449.

9 D.-H. Guan, X.-X. Wang, M.-L. Li, F. Li, L.-J. Zheng, X.-L. Huang and J.-J. Xu, *Angew. Chem., Int. Ed.*, 2020, **59**, 19518.

10 X. Sun, X. Mu, W. Zheng, L. Wang, S. Yang, C. Sheng, H. Pan, W. Li, C.-H. Li, P. He and H. Zhou, *Nat. Commun.*, 2023, **14**, 536.

11 T. Jian, W. Ma, C. Xu, H. Liu and J. Wang, *eScience*, 2023, **3**, 100114.

12 Y.-F. Wang, G.-J. Ji, L.-N. Song, X.-X. Wang and J.-J. Xu, *ACS Energy Lett.*, 2023, **8**, 1026.

13 Y. Qiao, S. Xu, Y. Liu, J. Dai, H. Xie, Y. Yao, X. Mu, C. Chen, D. J. Kline, E. M. Hitz, B. Liu, J. Song, P. He, M. R. Zachariah and L. Hu, *Energy Environ. Sci.*, 2019, **12**, 1100.

14 J. Chen, X.-Y. Chen, Y. Liu, Y. Qiao, S.-Y. Guan, L. Li and S.-L. Chou, *Energy Environ. Sci.*, 2023, **7**, 130.

15 C. Yang, K. Guo, D. Yuan, J. Cheng and B. Wang, *J. Am. Chem. Soc.*, 2020, **142**, 6983.

16 X. Ma, W. Zhao, Q. Deng, X. Fu, L. Wu, W. Yan and Y. Yang, *J. Power Sources*, 2022, **535**, 231446.

17 D.-H. Guan, X.-X. Wang, F. Li, L.-J. Zheng, M.-L. Li, H.-F. Wang and J.-J. Xu, *ACS Nano*, 2022, **16**, 12364.

18 X.-X. Wang, D.-H. Guan, F. Li, M.-L. Li, L.-J. Zheng and J.-J. Xu, *Small*, 2021, **17**, 2100642.

19 B. Chen, D. Wang, J. Tan, Y. Liu, M. Jiao, B. Liu, N. Zhao, X. Zou, G. Zhou and H.-M. Cheng, *J. Am. Chem. Soc.*, 2022, **144**, 3106.

20 S. Yang, P. He and H. Zhou, *Energy Environ. Sci.*, 2016, **9**, 1650.

21 Z. Guo, J. Li, H. Qi, X. Sun, H. Li, A. G. Tamirat, J. Liu, Y. Wang and L. Wang, *Small*, 2019, **15**, e1803246.

22 C. Wang, Q. Zhang, X. Zhang, X.-G. Wang, Z. Xie and Z. Zhou, *Small*, 2018, **14**, e1800641.

23 S. Yang, Y. Qiao, P. He, Y. Liu, Z. Cheng, J.-j. Zhu and H. Zhou, *Energy Environ. Sci.*, 2017, **10**, 972.

24 H. Zhao, D. Li, H. Li, A. G. Tamirat, X. Song, Z. Zhang, Y. Wang, Z. Guo, L. Wang and S. Feng, *Electrochim. Acta*, 2019, **299**, 592.

25 S. Thoka, C.-J. Chen, A. Jena, F.-M. Wang, X.-C. Wang, H. Chang, S.-F. Hu and R.-S. Liu, *ACS Appl. Mater. Interfaces*, 2020, **12**, 17353.

26 A. Hu, C. Shu, C. Xu, R. Liang, J. Li, R. Zheng, M. Li and J. Long, *J. Mater. Chem. A*, 2019, **7**, 21605.

27 X.-X. Wang, G.-J. Ji, P. She, F. Li, Q.-C. Liu, H.-F. Wang and J.-J. Xu, *Chem. Eng. J.*, 2021, **426**, 131101.

28 X. Chen, J. Chen, Y. Liu, Y. Liu, Y. Gao, S. Fan, X. He, X. Liu, C. Shen, Y. Jiang, L. Li, Y. Qiao and S. Chou, *ACS Appl. Mater. Interfaces*, 2023, **15**, 28106.

29 D. Lei, S. Ma, Y. Lu, Q. Liu and Z. Li, *J. Electron. Mater.*, 2019, **48**, 4653–4659.

30 Q. Liu, Z. Hu, L. Li, W. Li, C. Zou, H. Jin, S. Wang and S.-L. Chou, *ACS Appl. Mater. Interfaces*, 2021, **13**, 16585.

31 B. Ge, Y. Sun, J. Guo, X. Yan, C. Fernandez and Q. Peng, *Small*, 2019, **15**, e1902220.

32 Y. Mao, C. Tang, Z. Tang, J. Xie, Z. Chen, J. Tu, G. Cao and X. Zhao, *Energy Storage Mater.*, 2019, **18**, 405.

33 Z. Tang, M. Yuan, H. Zhu, G. Zeng, J. Liu, J. Duan and Z. Chen, *Front. Chem.*, 2021, **9**, 670612.

34 Q. Deng, Y. Yang, S. Qu, W. Wang, Y. Zhang and X. Ma, *Energy Storage Mater.*, 2021, **42**, 484.

35 J. Xia, Y. Zhou, J. Zhang, T. Lu, W. Gong, D. Zhang, X. Wang and J. Di, *Small*, 2023, **19**, 2301906.

36 X. Guo, T. Zheng, G. Ji, N. Hu, C. Xu and Y. Zhang, *J. Mater. Chem. A*, 2018, **6**, 10243.

37 M. Al-Dossary, A. A. Ismail, J. L. G. Fierro, H. Bouzid and S. A. Al-Sayari, *Appl. Catal., B*, 2015, **165**, 651.

38 J. Chen, X. Qi, C. Liu, J. Zeng and T. Liang, *ACS Appl. Mater. Interfaces*, 2020, **12**, 51418.

39 W. Ma, S. Lu, X. Lei, X. Liu and Y. Ding, *J. Mater. Chem. A*, 2018, **6**, 20829.

40 X. Zhang, C. Wang, H. Li, X.-G. Wang, Y.-N. Chen, Z. Xie and Z. Zhou, *J. Mater. Chem. A*, 2018, **6**, 2792.

41 L. Liu, L. Zhang, K. Wang, H. Wu, H. Mao, L. Li, Z. Sun, S. Lu, D. Zhang, W. Yu and S. Ding, *ACS Appl. Mater. Interfaces*, 2020, **12**, 33846.

42 S. Thoka, C.-J. Chen, A. Jena, F.-M. Wang, X.-C. Wang, H. Chang, S.-F. Hu and R.-S. Liu, *ACS Appl. Mater. Interfaces*, 2020, **12**, 17353.

43 Y. Qiao, J. Wu, J. Zhao, Q. Li, P. Zhang, C. Hao, X. Liu, S. Yang and Y. Liu, *Energy Storage Mater.*, 2020, **27**, 133.

44 D. Na, H. Jeong, J. Baek, H. Yu, S.-M. Lee, C.-R. Lee, H.-K. Seo, J.-K. Kim and I. Seo, *Electrochim. Acta*, 2022, **419**, 140408.

45 A. Bharti, G. Manna, P. Saha, G. Achutarao and A. J. Bhattacharyya, *J. Phys. Chem. Lett.*, 2022, **13**, 7380.

46 W. Ma, S. Lu, X. Lei, X. Liu and Y. Ding, *J. Mater. Chem. A*, 2018, **6**, 20829.

47 H. Liao, X. Guo, Y. Hou, H. Liang, Z. Zhou and H. Yang, *Small*, 2020, **16**, e1905223.